A critical investigation of γ-heating rates in stellar matter

Musarat Abbas† Jameel-Un Nabi Arslan Mehmood

University of Wah, Quaid Avenue, Wah Cantt 47040, Punjab, Pakistan

Abstract: The simulation of observed properties of type I X-ray bursts, also known as superbursts, poses challenges once we include Cooper pair neutrinoemission from the crust of the neutron star. An additional heating of theaccumulating fuel layer is in order. γ-emission due to electron captures to excited states in astrophysical environments is a major source to make up for the heat loss carried away by the weak-interaction neutrinos. γ-heating is believed to have a significant impact during the presupernova evolution of massive stars and calculation of the thermal structure in the crust and core of a superbursts. This deposition of energy enhances entropy production and promotes convection at this stage of stellar evolution. Effective γ-heating rates may contribute to reduction of the ignition depth of superbursts. A recent investigation ranked the leading electron capturing nuclei causing significant changes in the lepton-to-baryon fraction (Y_e) of the stellar matter after silicon core burning. We investigate γ-heating rates from the excited states of the top 100 electron capture and positron decay nuclei identified in recently published ranking list. To assess the influence of γ-heating rates, each nucleus was analyzed using four different empirical pairing gaps and three distinct sets of nuclear deformation parameters. We report our calculations for the temperature range [(1 - 10) GK] and density range [(10^9 - 10^{11}) g/cm^3]. The calculated γ-heating rates changed up to a factor 26 (16) with changing deformation values (pairing gaps). Our findings may contribute to a more realistic simulations of post-silicon burning phases of massive stars and superbursting neutron stars.

Keywords: γ-heating rates, nuclear deformation, pairing gaps, GT strength distributions, pn-QRPA model

DOI: **CSTR:**

I. INTRODUCTION

The mechanism of energy generation within stars [1], nucleosynthesis [2], and the dynamics of supernova explosions [3] continue to be active areas of research in astrophysics. A complete understanding of these phenomena is essential for a reliable modeling of the evolution of the universe. It was concluded in an earlier study [4] that inefficient core and crust neutrino emissions along with a poor crust thermal conductivity are prerequisites for a superbursting neutron star, commonly referred to as superbursts. It was inferred that the superburst ignition column depths were too large as a result of neutrino cooling by Cooper pairing of neutrons in the crust. It was further suggested that an extra heating mechanism was required in superburst models to simulate the observed data. The earliest cooling phases of a neutron star are dominated by neutrino emissions whereas subsequent cooling is attributed to thermal radiation from the surface. Neutrino cooling reduces the interior temperature of neutron stars to $\geq 10^9$ K. For temperatures beyond 10^{10} K, the dominant neutrino emission processes are the modified Urca process and neutrino pair bremsstrahlung in nucleon-nucleon collisions. Flowers et al. [5] calculated neutrino emission process in the temperature range (10^9 -10^{10}) K for neutron fluid that has transitioned to the superfluid state. At any nonzero temperature $T < T_c$ (critical temperature) the neutron fluid has two components: a superfluid condensate and quasiparticle excitations. The latter component arises due to broken "Cooper pairs". The authors calculated the neutrino pair emissivity due to the recombination of broken pairs that then join the condensate resulting in the emission of neutrino-antineutrino pairs. The authors concluded that in the temperature range (10^9 -10^{10}) K, the recombination emissivity can dominate all other cooling mechanisms. Superbursts, thought to be a thermonuclear runaway initially caused by carbon unstable burning, possess ignition depths deeper than that of the H/He ignition. Both neutron stars and X-ray bursts are affected by neutrino cooling mechanisms. Superbursts should be affected by neutrino losses at relatively deeper layer inside neutron stars compared with usual X-ray bursts [4, 6]. In particular, the impacts of neutrino cooling on the recurrence time of superbursts strongly de-

Received 7 November 2025; Accepted 28 February 2026

† E-mail: abbaschk87@gmail.com (Musarat Abbas)

pend on the thermal neutrino losses (e.g., [6]) for nucleon-pair bremsstrahlung and crust Cooper pair breaking and formation process. Gupta et al. [6] performed a self-consistent calculation of the thermal structure of superbursts. The authors demonstrated that allowing electron captures to proceed through excited nuclear states led to a significant increase in the thermal energy released within the outer crust of accreting neutron stars. This process greatly offsets the fraction of reaction energy carried away by neutrinos. While neutrinos freely escape and remove substantial energy from the transparent core at such densities, γ-rays become trapped inside and deposit energy, thereby heating the stellar material. The interplay between neutrino cooling and γ-heating contributes to oxygen deflagration and helps trigger convective motion in the core. They further emphasized that the resulting crustal heating is highly sensitive to the initial nuclear composition formed during the burning of lighter elements in the neutron star's envelope. This sensitivity arose from strong shell and subshell effects in neutron-rich nuclei, which triggered notable changes in nuclear shape, single-particle structure, and electron-capture strength distributions, even for nuclei with comparable proton and mass numbers. Gupta and collaborators computed up to a factor of 10 bigger γ-heating rates at densities $\leq 10^{11}$ g/cm^3 than previously estimated. These higher γ-heating rates were suggested to shorten the ignition column depths counteracting the effect of reduction in temperature from Cooper pairing of neutrons in the crust. The higher calculated γ-heating rates further supported the reduction in the discrepancy between the temperatures needed for unstable ^{12}C ignition on timescales consistent with the observations. It was concluded that crustal heating calculations were very sensitive to the underlying nuclear physics. The authors stressed on a reliable calculation of the nuclear structure and β-decay properties of very neutron-rich nuclei up to mass number 106. Such a calculation may constrain the lowest lying electron capture strength, which in turn determines the γ-heating rates.

During the final stages of a massive star's life cycle, weak-interaction processes are significantly influenced by charge-exchange mechanisms, also referred to as Gamow-Teller (GT) transitions [7]. These reactions, governed by the weak force, subsequently lead to γ-heating and neutrino cooling rates. Key processes in stellar core collapse, including magnetorotational instabilities [8], electron capture (EC) on nuclei and the resulting γ-heating are highly temperature-dependent. As collapse proceeds, the stellar core is compressed to nuclear densities, after which it rebounds against the stiff nuclear matter. This rebound drives the ejection of parts of the heavy-element core along with the outer shells into the interstellar medium [9]. At this stage, γ-heating may also assist in re-energizing the stalled shock, thereby supporting explosive burning and driving convection. In the late evolutionary stages of massive stars, weak interaction processes play a decisive role in regulating the core's energy balance.

Nuclear shapes and pairing gaps are two crucial parameters used to investigate various nuclear structure properties including those possessing astrophysical significance. Experimental studies of atomic nuclei have revealed that they can adopt various shapes, such as spherical or ellipsoidal. In many cases, the ellipsoidal configurations exhibit significant deviations from the ideal spherical form known as deformations. Such nuclear deformations are particularly prominent in nuclei far from the magic numbers associated with enhanced stability. As nuclei moves away from the stability line, weaker nucleon binding and a greater imbalance between protons and neutrons result in substantial alterations to the nuclear potential. The spin–isospin component of the nucleon–nucleon interaction further influences these effects by modifying the single-particle energy levels. Combined with the growing importance of many-body correlations amplify these effects, resulting in the breakdown of conventional shell closures and the emergence of new ones. The evolution of nuclear shapes across different regions of the nuclear chart remains an active area of research, investigated through a wide range of experimental [10, 11] and theoretical approaches [12−14]. At the same time, a better understanding of the nucleon pairing effect in nuclear matter is pivotal for interpreting a spectrum of astrophysical phenomena associated with compact stellar objects. These include the thermal evolution of nascent neutron stars [15], post-outburst relaxation dynamics in X-ray bursts [16], and pulsar glitch dynamics [17, 18].

A robust theoretical characterization of pairing correlations necessitates the incorporation of precise bare nucleon-nucleon interactions. Nevertheless, the magnitude and behavior of pairing gaps within nuclear matter remain constrained [19], posing a significant challenge to predictive modeling efforts.

Several theoretical studies have been conducted in the past to investigate the effect of temperature on nuclear properties (e.g., [20−32]. Pairing of nucleons was neglected in the calculations for hot giant dipole resonance (GDR) as it was believed that the gap vanishes at $T = T_c < 1$ MeV according to the BCS theory. It was later discovered that thermal fluctuations smear out the superfluid-normal phase transition in finite systems so that the pairing gap survives up to $T \gg 1$ MeV [28]. It was shown that the effect of thermal pairing causes a smaller GDR width at $T \leq 2$ MeV as compared to the one obtained by neglecting pairing [24]. Other approaches also support the argument that pairing correlations do not abruptly disappear at $T \neq 0$ [29−31]. It was suggested in Ref. [33] that the decrease of the pairing gap with increasing temperature, which is also caused by particle-particle and

hole-hole configurations at low temperatures, may slow down the increase of the GDR width. An investigation conducted to study the temperature dependence of the pairing gap beyond the BCS approximation led to noticeably higher values of the critical temperature [26]. The equation of motion for the two-fermion two-time correlation function in the pairing channel was considered at finite temperature for ^{68}Ni, ^{44}Ca and ^{46}Ca. It was concluded that in the pure BCS case, the pairing gap decreased quickly with the temperature increase and disappeared around T = 1.2 MeV. However, in the BCS + particle-vibration coupling calculation, the gap values were still significant around T= 1 MeV. The pairing gap retained its peaked character in the BCS + particle-vibration coupling calculation even when its average value decreased with a rise in temperature. Authors explored the nuclear shell structure of nickel isotopes in a finite-temperature relativistic framework [27]. In these calculations pairing correlations were considered up to temperature of 1 MeV.

One of the noticeable works regarding finite temperature investigation of nuclear properties was reported by Ravlić et al. [32]. The authors presented the mapping of nuclear drip lines at temperatures up to T =20 GK using the relativistic energy density functional theory, including treatment of thermal scattering of nucleons in the continuum. The authors did not incorporate approaches beyond the mean field nor account for statistical (thermal) fluctuations in their calculations. The findings of their work stated that the pairing gaps and deformation properties are present at least up to T= 10 GK (~ 1 MeV). They commented that for temperatures beyond 1 MeV, these two nuclear structure properties may still exist provided thermal fluctuations are considered. The authors reported that for temperatures $T \leq$ 12 GK, the interplay between the properties of nuclear effective interaction, pairing, and temperature effects determine the nuclear binding. At higher temperatures, the pairing correlations disappear, shell effects vanish, and a transition occurs from the superfluid to the normal states. The authors commented that the nuclear deformation decreased with temperature, leading to a transition from the deformed to the spherical state. At T = 1 MeV, the authors found a significant number of nuclei exhibiting deformation effects. It may be safely concluded from the above arguments that pairing and deformation effects do exist at least up to T= 10 GK. Consequently, we present our calculations on effects of pairing gaps and nuclear deformation on γ-heating rates only up to T= 10 GK (~ 1 MeV).

We used the proton-neutron Quasiparticle Random Phase Approximation (pn-QRPA) model [34] to calculate the γ-heating rates in stellar environment. Our nuclear model did not consider the smearing of Fermi surface due to heating effects. However, we do consider the smearing of the nuclear Fermi-surface because of pairing correlation in our current calculation. There are studies based on QRPA formalism that include the effect of finite temperature in the calculation of nuclear matrix elements (NMEs) of Fermi and GT transitions. The studies performed by Dzhioev and collaborators [35] were based on TQRPA approach in which temperature is taken into account within the thermo-field dynamics formalism by using the Woods-Saxon potential, BCS pairing interactions and separable multipole and spin-multipole particle-hole interactions. The TQRPA allows the determination of temperature-dependent spectral functions and treats the ground state and thermally excited states consistently on the level of 2p-2h correlations. A self-consistent FTQRPA approach within relativistic [36] and non-relativistic [37] frameworks, based on nuclear energy density functionals for evaluation of nuclear weak interaction rates, is also available at finite temperature. The evolution of the GT_+ spectrum with temperature was investigated using the finite-temperature proton-neutron relativistic time blocking approximation and the finite-temperature proton-neutron relativistic random phase approximation models [38]. The calculations showed only minor changes in the GT_+ distributions for the nuclei around ^{78}Ni when temperature increased from 0 to around 1 MeV [38]. The relativistic and nonrelativistic finite temperature proton-neutron quasiparticle random phase approximation methods were developed to study the interplay of the pairing and temperature effects on the GT excitations in open-shell nuclei [39]. The findings showed that pairing effects are crucial for a proper description of the spin-isospin excitations, especially at temperatures below 1 MeV and further concluded that the thermal evolution of the GT_- spectrum for ^{42}Ca, ^{46}Ti and ^{118}Sn displayed small changes up to temperature of 1 MeV. On the other hand, our model also has an advantage which makes our calculation of reduced transition probabilities more reliable than other nuclear models. Our model is perhaps one of the very few models that calculate GT strength distributions from parent ground and low-lying excited states (up to 10 MeV) in a microscopic fashion. Other models (e.g., [40−45]) calculate the GT distributions from the ground state (and perhaps a few low-lying states up to 1-2 MeV) and for the remaining parent levels assume the Brink-Axel hypothesis [46, 47]. The Brink-Axel hypothesis is not a good approximation for estimating excited state GT distribution functions [48].

Based on a simulation study of presupernova evolution, Nabi et al. [49] identified a suite of crucial electron capture nuclei whose reaction rates most significantly influenced the dynamics of stellar core collapse. The authors selected an ensemble consisting of 728 nuclei with mass range of A = (1 - 100) and adopted a novel recipe for computation of nuclear partition functions. The capture rates on these nuclei directly govern the core's lepton fraction rate ($\dot{Y}_e$) and entropy, thereby playing a funda-

mental role in the initial collapse dynamics and the subsequent supernova mechanism. The authors published an updated list of electron capturing nuclei which had the largest effect on $\dot{Y}_e$ for conditions after silicon core burning. We selected the top 100 electron capturing nuclei for the current investigation of γ-heating rates.

The γ-heating rates for the top 100 EC nuclei were calculated using four different pairing-gap prescriptions, namely: (i) Lipkin–Nogami ($\Delta^{(\mathrm{LN})}$) [50]; (ii) Madland–Nix ($\Delta^{(\mathrm{MN})}$) [51]; (iii) the four-point ($\Delta^{(4)}$) [52]; and the five-point ($\Delta^{(5)}$) [52] empirical pairing models. Additionally, three sets of nuclear deformation parameters, corresponding to β_2 values from the FRLDM (1981) [53], FRDM (1992) [54], and FRDM (2012) [55] models, were employed as input parameters in our nuclear model to investigate their effects on computed γ-heating rates.

This paper is organized as follows. Section 2 outlines the theoretical framework for the calculation of γ-ray heating energy rates. Section 3 presents and discusses the calculated results in depth and presents a comparison with the available measured data. Finally, Section 4 provides a concise summary of the main conclusions and implications of the present investigation.

II. FORMALISM

The central idea of the current study is to investigate the effects of nuclear shape and nucleon pairing gaps on the computed γ-heating rates. The charge-changing transitions were calculated using the pn-QRPA model with a simple pairing plus quadrupole Hamiltonian with the incorporation of particle-particle (pp) and particle-hole (ph) GT forces of separable form. We began with a spherical single-particle basis ($s^{\dagger}_{jm}$, s_{jm}) and introduced an axially symmetric deformation which generated the corresponding canonical (Nilsson) basis ($D^{\dagger}_{m\alpha}$, $D_{m\alpha}$).

$$D^{\dagger}_{m\alpha} = \sum_{j} T^{m}_{j\alpha}\, s^{\dagger}_{jm}, \tag{1}$$

where m denotes the projection of angular momentum onto the symmetry axis, while α represents additional quantum numbers to determine the states completely. The transformation matrix T consisted of Nilsson eigenfunctions within the Nilsson+BCS model. The quasiparticle (Q) basis was defined using yet another transformation, expressed as

$$Q^{\dagger}_{m\alpha} = u_{m\alpha}\, D^{\dagger}_{m\alpha} - v_{m\alpha}\, D_{\bar{m}\alpha} \tag{2}$$

$$Q^{\dagger}_{\bar{m}\alpha} = u_{m\alpha}\, D^{\dagger}_{\bar{m}\alpha} + v_{m\alpha}\, D_{m\alpha}, \quad (m > 0), \tag{3}$$

where $\bar{m}$ denotes the time reversed state of m. The occupation amplitude satisfies the condition $u^2_{m\alpha} = v^2_{m\alpha} = 1$. We employed the BCS theory to determine the values of u and v. The pn-QRPA phonons creation operators $\hat{\Phi}$ were expressed as

$$\hat{\Phi}^{\dagger}_{\Psi}(\mu) = \sum_{pn} X^{pn}_{\Psi}(\mu)\hat{Q}^{\dagger}_{p}\hat{Q}^{\dagger}_{\bar{n}} - Y^{pn}_{\Psi}(\mu)\hat{Q}_{n}\hat{Q}_{\bar{p}}\,, \tag{4}$$

The indices n and p distinguished between the single quasi-particle states of the neutron and the proton and stands for $m_p\alpha_p$ and $m_n\alpha_n$, respectively. The sum fulfilled the conditions $\mu = m_p - m_n = 0, \pm 1$ and $\pi_p.\pi_n = 1$ for neutrons and protons pairs. The term Ψ denotes the energy eigenvalues whereas forward- and backward-amplitudes (X) and (Y) are the eigenfunctions of the RPA equation for proton-neutron quasiparticle pair states

$$\begin{bmatrix} M & N \\ -N & -M \end{bmatrix} \begin{bmatrix} X \\ Y \end{bmatrix} = \Psi \begin{bmatrix} X \\ Y \end{bmatrix}. \tag{5}$$

The RPA equations were solved separately for each values of μ. Details of the elements of the submatrices M and N can be seen from Ref. [56].

A. Extension to odd-odd and odd-A mass nuclei

Initially, the RPA framework was employed to calculate excitation states from the ground state of even–even nuclei. Subsequently, the authors in Ref. [56] extended the model to odd–odd and odd-A systems. For odd-A nuclei, two types of transitions are possible. The first corresponds to a phonon excitation in which the odd particle does not take part in the interaction, while the second type involves transition between one-quasiparticle states. Phonon correlations were incorporated in the one-quasiparticle configurations using first-order perturbation theory

$$|p_{corr}\rangle = Q^{\dagger}_{p}|-\rangle + \sum_{n,\Psi} Q^{\dagger}_{n}\hat{\Phi}^{\dagger}_{\Psi}(\mu)|-\rangle \times \langle -|[Q^{\dagger}_{n}\hat{\Phi}^{\dagger}_{\Psi}(\mu)]^{\dagger} H_{31} Q^{\dagger}_{p}|-\rangle \times E_{p}(n,\Psi), \tag{6}$$

$$|n_{corr}\rangle = Q^{\dagger}_{n}|-\rangle + \sum_{p,\Psi} Q^{\dagger}_{p}\hat{\Phi}^{\dagger}_{\Psi}(-\mu)|-\rangle \times \langle -|[Q^{\dagger}_{p}\hat{\Phi}^{\dagger}_{\Psi}(-\mu)]^{\dagger} H_{31} Q^{\dagger}_{n}|-\rangle \times E_{n}(p,\Psi), \tag{7}$$

$$E_{i}(j,\Psi) = \frac{1}{\epsilon_{i} - \epsilon_{j} - \Psi}, (i,j = p,n), \tag{8}$$

where ϵ denotes the quasi-particle energies. The quasi-particle-phonon coupled Hamiltonian term H_{31} in Eqs. 6 and 7 was defined using the relation

$$
\begin{aligned}
H_{31} = & \sum V_{pn,\bar{p'}n'}(u_p u_n v_{p'} u_{n'} - v_p v_n u_{p'} v_{n'}) \\
& \times (Q_p^\dagger Q_n^\dagger Q_{p'}^\dagger Q_{n'} + h.c.) \\
& + \sum V_{pn,p'\bar{n'}}(v_p v_n v_{p'} u_{n'} - u_p u_n u_{p'} v_{n'}) \\
& \times (Q_p^\dagger Q_n^\dagger Q_{n'}^\dagger Q_{p'} + h.c.) \,, \qquad (9)
\end{aligned}
$$

where the Hermitian conjugate ($h.c$) terms ensure proper symmetry of the operators. V denotes the two-body interaction matrix elements. The explicit form of V for a separable and schematic interaction as well as the charge-changing transition amplitudes between correlated one-quasiparticle states can be seen from Ref. [56]. The idea of quasiparticle transitions with first-order phonon correlations can be extended to an odd-odd parent nucleus. The ground state is assumed to be a proton–neutron quasiparticle pair state of the smallest energy. The GT transitions of the quasiparticle lead to two-proton or two-neutron quasiparticle states in the daughter nucleus. The two-quasiparticle states were constructed with phonon correlations and were given by

$$
\begin{aligned}
|pn_{corr}> = & Q_p^\dagger Q_n^\dagger|-> + \frac{1}{2}\sum_{p'_1,p'_2,\Psi} Q_{p'_1}^\dagger Q_{p'_2}^\dagger \hat{\Phi}_\Psi^\dagger(-\mu)|-> \times <-|[Q_{p'_1}^\dagger Q_{p'_2}^\dagger \hat{\Phi}_\Psi^\dagger(-\mu)]^\dagger H_{31} Q_p^\dagger Q_n^\dagger|-> E_{pn}(p'_1 p'_2, \Psi) \\
& + \frac{1}{2}\sum_{n'_1,n'_2,\Psi} Q_{n'_1}^\dagger Q_{n'_2} \hat{\Phi}_\Psi^\dagger(\mu)|-> \times <-|[Q_{n'_1}^\dagger Q_{n'_2}^\dagger \hat{\Phi}_\Psi^\dagger(\mu)]^\dagger H_{31} Q_p^\dagger Q_n^\dagger|-> E_{pn}(n'_1 n'_2, \Psi) \,, \qquad (10)
\end{aligned}
$$

$$
< p_1 p_{2corr}| = Q_{p_1}^\dagger Q_{p_2}^\dagger|-> + \sum_{p',n',\Psi} Q_{p'}^\dagger Q_{n'}^\dagger \hat{\Phi}_\Psi^\dagger(\mu)|-> \times <-|[Q_{p'}^\dagger Q_{n'}^\dagger \hat{\Phi}_\Psi^\dagger(\mu)]^\dagger H_{31} Q_{p_1}^\dagger Q_{p_2}^\dagger|-> E_{p_1 p_2}(p'n', \Psi) \,, \qquad (11)
$$

$$
< n_1 n_{2corr}| = Q_{n_1}^\dagger Q_{n_2}^\dagger|-> + \sum_{p',n',\Psi} Q_{p'}^+ Q_{n'}^\dagger \hat{\Phi}_\Psi^\dagger(-\mu)|-> \times <-|[Q_{p'}^\dagger Q_{n'}^\dagger \hat{\Phi}_\Psi^\dagger(-\mu)]^\dagger H_{31} Q_{n_1}^\dagger Q_{n_2}^\dagger|-> E_{n_1 n_2}(p'n', \Psi) \,, \qquad (12)
$$

where

$$
E_{ab}(cd, \Psi) = \frac{1}{(\epsilon_a + \epsilon_b) - (\epsilon_c + \epsilon_d + \Psi)} \qquad (13)
$$

These two-quasiparticle states were expressed in terms of one-quasiparticle transition amplitudes using the following relations

$$
\begin{aligned}
& < p_1 p_{2corr}|\tau_\pm \sigma_\mu|pn_{corr}> \\
= & \, \delta(p_1, p) < p_{2corr}|\tau_\pm \sigma_\mu|n_{corr}> \\
& - \delta(p_2, p) < p_{1corr}|\tau_\pm \sigma_\mu|n_{corr}> \,, \qquad (14)
\end{aligned}
$$

$$
\begin{aligned}
& < n_1 n_{2corr}|\tau_\pm \sigma_{-\mu}|pn_{corr}> \\
= & \, \delta(n_2, n) < n_{1corr}|\tau_\pm \sigma_{-\mu}|p_{corr}> \\
& - \delta(n_1, n) < n_{2corr}|\tau_\pm \sigma_{-\mu}|p_{corr}> \,, \qquad (15)
\end{aligned}
$$

When a nucleus contains an odd nucleon, the low-lying excited states are generated by promoting the quasiparticle from the lowest-energy orbital to higher-lying orbitals. For odd-proton even-neutron nuclei, these excited states can be described either as three-proton configurations or as one-proton–two-neutron configurations, corresponding to excitations of a proton or a neutron, respectively

$$
\begin{aligned}
|p_1 p_2 p_{3corr}\rangle = & Q_{p_1}^\dagger Q_{p_2}^\dagger Q_{p_3}^\dagger|-\rangle + \frac{1}{2}\sum_{p'_1,p'_2,n',\Psi} Q_{p'_1}^\dagger Q_{p'_2}^\dagger Q_{n'}^\dagger \hat{\Phi}_\Psi^\dagger(\mu)|-\rangle \\
& \times \langle -|[Q_{p'_1}^\dagger Q_{p'_2}^\dagger Q_{n'}^\dagger \hat{\Phi}_\Psi^\dagger(\mu)]^\dagger H_{31} Q_{p_1}^\dagger Q_{p_2}^\dagger Q_{p_3}^\dagger|-\rangle E_{p_1 p_2 p_3}(p'_1 p'_2 n', \Psi) \,, \qquad (16)
\end{aligned}
$$

$$
\begin{aligned}
|p_1 n_1 n_{2corr}\rangle &= Q^{\dagger}_{p_1} Q^{\dagger}_{n_1} Q^{\dagger}_{n_2}|-\rangle + \frac{1}{2}\sum_{p'_1,p'_2,n',\Psi} Q^{\dagger}_{p'_1} Q^{\dagger}_{p'_2} Q^{\dagger}_{n'} \hat{\Phi}^{\dagger}_{\Psi}(-\mu)|-\rangle \times \langle -|[Q^{\dagger}_{p'_1} Q^{\dagger}_{p'_2} Q^{\dagger}_{n'} \hat{\Phi}^{\dagger}_{\Psi}(-\mu)]^{\dagger} H_{31} Q^{\dagger}_{p_1} Q^{\dagger}_{n_1} Q^{\dagger}_{n_2}|-\rangle \\
&\times E_{p_1 n_1 n_2}(p'_1 p'_2 n', \Psi) + \frac{1}{6}\sum_{n'_1,n'_2,n'_3,\Psi} Q^{\dagger}_{n'_1} Q^{\dagger}_{n'_2} Q^{\dagger}_{n'_3} \hat{\Phi}^{\dagger}_{\Psi}(\mu)|-\rangle \\
&\times \langle -|[Q^{\dagger}_{n'_1} Q^{\dagger}_{n'_2} Q^{\dagger}_{n'_3} \hat{\Phi}^{\dagger}_{\Psi}(\mu)]^{\dagger} H_{31} Q^{\dagger}_{p_1} Q^{\dagger}_{n_1} Q^{\dagger}_{n_2}|-\rangle E_{p_1 n_1 n_2}(n'_1 n'_2 n'_3, \Psi)\,, \qquad (17)
\end{aligned}
$$

with the energy denominators of first order perturbation

$$
E_{abc}(def, \Psi) = \frac{1}{(\epsilon_a + \epsilon_b + \epsilon_c - \epsilon_d - \epsilon_e - \epsilon_f - \Psi)}\,, \qquad (18)
$$

The transition amplitudes between three–quasiparticle states were reduced to effective amplitudes for correlated one–quasiparticle states

$$
\begin{aligned}
&\langle p'_1 p'_2 n'_{1corr}|\tau_{\pm}\sigma_{-\mu}|p_1 p_2 p_{3corr}\rangle \\
&= \delta(p'_1, p_2)\delta(p'_2, p_3)\langle n'_{1corr}|\tau_{\pm}\sigma_{-\mu}|p_{1corr}\rangle \\
&\quad - \delta(p'_1, p_1)\delta(p'_2, p_3)\langle n'_{1corr}|\tau_{\pm}\sigma_{-\mu}|p_{2corr}\rangle \\
&\quad + \delta(p'_1, p_1)\delta(p'_2, p_2)\langle n'_{1corr}|\tau_{\pm}\sigma_{-\mu}|p_{3corr}\rangle\,, \qquad (19)
\end{aligned}
$$

$$
\begin{aligned}
&\langle p'_1 p'_2 n'_{1corr}|\tau_{\pm}\sigma_{\mu}|p_1 n_1 n_{2corr}\rangle \\
&= \delta(n'_1, n_2)[\delta(p'_1, p_1)\langle p'_{2corr}|\tau_{\pm}\sigma_{\mu}|n_{1corr}\rangle \\
&\quad - \delta(p'_2, p_1)\langle p'_{1corr}|\tau_{\pm}\sigma_{\mu}|n_{1corr}\rangle] \\
&\quad - \delta(n'_1, n_1)[\delta(p'_1, p_1)\langle p'_{2corr}|\tau_{\pm}\sigma_{\mu}|n_{2corr}\rangle \\
&\quad - \delta(p'_2, p_1)\langle p'_{1corr}|\tau_{\pm}\sigma_{\mu}|n_{2corr}\rangle]\,, \qquad (20)
\end{aligned}
$$

$$
\begin{aligned}
&\langle n'_1 n'_2 n'_{3corr}|\tau_{\pm}\sigma_{-\mu}|p_1 n_1 n_{2corr}\rangle \\
&= \delta(n'_2, n_1)\delta(n'_3, n_2)\langle n'_{1corr}|\tau_{\pm}\sigma_{-\mu}|p_{1corr}\rangle \\
&\quad - \delta(n'_1, n_1)\delta(n'_3, n_2)\langle n'_{2corr}|\tau_{\pm}\sigma_{-\mu}|p_{1corr}\rangle \\
&\quad + \delta(n'_1, n_1)\delta(n'_2, n_2)\langle n'_{3corr}|\tau_{\pm}\sigma_{-\mu}|p_{1corr}\rangle\,, \qquad (21)
\end{aligned}
$$

and for parent nuclei with odd neutron

$$
\begin{aligned}
&\langle p'_1 n'_1 n'_{2corr}|\tau_{\pm}\sigma_{\mu}|n_1 n_2 n_{3corr}\rangle \\
&= \delta(n'_1, n_2)\delta(n'_2, n_3)\langle p'_{1corr}|\tau_{\pm}\sigma_{\mu}|n_{1corr}\rangle \\
&\quad - \delta(n'_1, n_1)\delta(n'_2, n_3)\langle p'_{1corr}|\tau_{\pm}\sigma_{\mu}|n_{2corr}\rangle \\
&\quad + \delta(n'_1, n_1)\delta(n'_2, n_2)\langle p'_{1corr}|\tau_{\pm}\sigma_{\mu}|n_{3corr}\rangle\,, \qquad (22)
\end{aligned}
$$

$$
\begin{aligned}
&\langle p'_1 n'_1 n'_{2corr}|\tau_{\pm}\sigma_{-\mu}|p_1 p_2 n_{1corr}\rangle \\
&= \delta(p'_1, p_2)[\delta(n'_1, n_1)\langle n'_{2corr}|\tau_{\pm}\sigma_{-\mu}|p_{1corr}\rangle \\
&\quad - \delta(n'_2, n_1)\langle n'_{1corr}|\tau_{\pm}\sigma_{-\mu}|p_{1corr}\rangle] \\
&\quad - \delta(p'_1, p_1)[\delta(n'_1, n_1)\langle n'_{2corr}|\tau_{\pm}\sigma_{-\mu}|p_{2corr}\rangle \\
&\quad - \delta(n'_2, n_1)\langle n'_{1corr}|\tau_{\pm}\sigma_{-\mu}|p_{2corr}\rangle]\,, \qquad (23)
\end{aligned}
$$

$$
\begin{aligned}
&\langle p'_1 p'_2 p'_{3corr}|\tau_{\pm}\sigma_{\mu}|p_1 p_2 n_{1corr}\rangle \\
&= \delta(p'_2, p_1)\delta(p'_3, p_2)\langle p'_{1corr}|\tau_{\pm}\sigma_{\mu}|n_{1corr}\rangle \\
&\quad - \delta(p'_1, p_1)\delta(p'_3, p_2)\langle p'_{2corr}|\tau_{\pm}\sigma_{\mu}|n_{1corr}\rangle \\
&\quad + \delta(p'_1, p_1)\delta(p'_2, p_2)\langle p'_{3corr}|\tau_{\pm}\sigma_{\mu}|n_{1corr}\rangle\,. \qquad (24)
\end{aligned}
$$

In odd–odd nuclei, low-lying excited states can be described within the quasiparticle framework as either proton–neutron pair configurations or as four–quasiparticle states formed by adding two protons or two neutrons. While transitions from two–quasiparticle states are treated separately, phonon-correlated four–quasiparticle states can be constructed in an analogous way to two– and three–quasiparticle configurations

$$
\begin{aligned}
&< p'_1 p'_2 n'_1 n'_{2corr}|\tau_{\pm}\sigma_{-\mu}|p_1 p_2 p_3 n_{1corr} > = \delta(n'_2, n_1)[\delta(p'_1, p_2)\delta(p'_2, p_3) < n'_{1corr}|\tau_{\pm}\sigma_{-\mu}|p_{1corr} > \\
&\quad - \delta(p'_1, p_1)\delta(p'_2, p_3) < n'_{1corr}|\tau_{\pm}\sigma_{-\mu}|p_{2corr} > + \delta(p'_1, p_1)\delta(p'_2, p_2) < n'_{1corr}|\tau_{\pm}\sigma_{-\mu}|p_{3corr} >] \\
&\quad - \delta(n'_1, n_1)[\delta(p'_1, p_2)\delta(p'_2, p_3) < n'_{2corr}|\tau_{\pm}\sigma_{-\mu}|p_{1corr} > - \delta(p'_1, p_1)\delta(p'_2, p_3) < n'_{2corr}|\tau_{\pm}\sigma_{-\mu}|p_{2corr} > \\
&\quad + \delta(p'_1, p_1)\delta(p'_2, p_2) < n'_{2corr}|\tau_{\pm}\sigma_{-\mu}|p_{3corr} >]\,, \qquad (25)
\end{aligned}
$$

$$
\begin{aligned}
&< p'_1p'_2p'_3p'_{4corr}|\tau_\pm\sigma_\mu|p_1p_2p_3n_{1corr} > = -\delta(p'_2,p_1)\delta(p'_3,p_2)\delta(p'_4,p_3) < p'_{1corr}|\tau_\pm\sigma_\mu|n_{1corr} > \\
&+\delta(p'_1,p_1)\delta(p'_3,p_2)\delta(p'_4,p_3) < p'_{2corr}|\tau_\pm\sigma_\mu|n_{1corr} > -\delta(p'_1,p_1)\delta(p'_2,p_2)\delta(p'_4,p_3) < p'_{3corr}|\tau_\pm\sigma_\mu|n_{1corr} > \\
&+\delta(p'_1,p_1)\delta(p'_2,p_2)\delta(p'_3,p_3) < p'_{4corr}|\tau_\pm\sigma_\mu|n_{1corr} > ;, \qquad (26)
\end{aligned}
$$

$$
\begin{aligned}
&< p'_1p'_2n'_1n'_{2corr}|\tau_\pm\sigma_\mu|p_1n_1n_2n_{3corr} > = \delta(p'_1,p_1)[\delta(n'_1,n_2)\delta(n'_2,n_3) < p'_{2corr}|\tau_\pm\sigma_\mu|n_{1corr} > \\
&-\delta(n'_1,n_1)\delta(n'_2,n_3) < p'_{2corr}|\tau_\pm\sigma_\mu|n_{2corr} > +\delta(n'_1,n_1)\delta(n'_2,n_2) < p'_{2corr}|\tau_\pm\sigma_\mu|n_{3corr} >] \\
&-\delta(p'_2,p_1)[\delta(n'_1,n_2)\delta(n'_2,n_3) < p'_{1corr}|\tau_\pm\sigma_\mu|n_{1corr} > -\delta(n'_1,n_1)\delta(n'_2,n_3) < p'_{1corr}|\tau_\pm\sigma_\mu|n_{2corr} > \\
&+\delta(n'_1,n_1)\delta(n'_2,n_2) < p'_{1corr}|\tau_\pm\sigma_\mu|n_{3corr} >] , \qquad (27)
\end{aligned}
$$

$$
\begin{aligned}
&< n'_1n'_2n'_3n'_{4corr}|\tau_\pm\sigma_{-\mu}|p_1n_1n_2n_{3corr} > = +\delta(n'_2,n_1)\delta(n'_3,n_2)\delta(n'_4,n_3) < n'_{1corr}|\tau_\pm\sigma_{-\mu}|p_{1corr} > \\
&-\delta(n'_1,n_1)\delta(n'_3,n_2)\delta(n'_4,n_3) < n'_{2corr}|\tau_\pm\sigma_{-\mu}|p_{1corr} > +\delta(n'_1,n_1)\delta(n'_2,n_2)\delta(n'_4,n_3) < n'_{3corr}|\tau_\pm\sigma_{-\mu}|p_{1corr} > \\
&-\delta(n'_1,n_1)\delta(n'_2,n_2)\delta(n'_3,n_3) < n'_{4corr}|\tau_\pm\sigma_{-\mu}|p_{1corr} > . \qquad (28)
\end{aligned}
$$

The anti-symmetrization of the quasi-particles was duly taken into account for each of these amplitudes.

$$
\begin{aligned}
&p'_4 > p'_3 > p'_2 > p'_1; n'_4 > n'_3 > n'_2 > n'_1; \\
&p_4 > p_3 > p_2 > p_1; n_4 > n_3 > n_2 > n_1.
\end{aligned}
$$

The GT transitions were taken into account for each phonon's excited state. It was assumed that the quasi-particle in the parent nucleus occupied the same orbit as the excited phonon. Further details of the formalism may be seen from Ref. [56].

The β decay partial half lives to daughter states, Ψ, were calculated using the relation

$$
t_\Psi = \frac{K}{f_V(Z,E,A)B_F(\Psi) + (g_V/g_A)^{-2} f_A(Z,E,A)B_{GT}(\Psi)}, \qquad (29)
$$

where E = (Q - Ψ), g_A/g_V = -1.254 [57] and K = 6143 s [58]. $f_A(Z,A,E)$ and $f_V(Z,A,E)$ are the integrals of the available phase space for axial vector and vector transitions, respectively. The phase space integrals were computed as per the recipe given in Ref. [59]. The reduced transition probabilities for GT and Fermi transitions are represented by B_{GT} and B_F, respectively. Details of calculation of nuclear matrix elements can be seen from Ref. [60]. The total β decay half-lives were computed by including all transition probabilities to the states in the daughter within the Q window and summing the partial half-lives in inverse relation

$$
T_{1/2} = \left(\sum_{0\le\Psi\le Q} \left(\frac{1}{t_\Psi}\right) \right)^{-1}. \qquad (30)
$$

The γ-heating rates, in stellar matter, were computed using the relation

$$
\lambda_\gamma = \sum_{ij} P_i E_j \lambda_{ij}, \qquad (31)
$$

where P_i is the occupation probability of the i^{th} parent state, E_j are the daughter energy levels and λ_{ij} represents the sum of electron capture (EC) and positron decay (PD) rates for transitions from parent state i to daughter level j

$$
\lambda_{ij} = K\left[f_{ij}^{EC} + f_{ij}^{PD}\right]\left[B(F_{ij}) + \left(\frac{g_A}{g_V}\right)^2 B(GT_{ij})\right]. \qquad (32)
$$

The first parenthesis on the right side of Eq. 32 are the phase-space integrals dependent on stellar temperature, density, and electron Fermi energy. These were computed using the relation (in natural units)

$$
f_{ij}^{PD} = \int_1^{\Psi_m} \Psi\sqrt{\Psi^2-1}\,(\Psi_m-\Psi)^3 F(-Z,\Psi)(1-D_+)\,d\Psi, \qquad (33)
$$

$$
f_{ij}^{EC} = \int_{\Psi_l}^{\infty} \Psi\sqrt{\Psi^2-1}\,(\Psi_m+\Psi)^3 F(Z,\Psi)D_-\,d\Psi, \qquad (34)
$$

where Ψ is the electron or positron energy, Ψ_m is the available total β-decay energy, Ψ_l is the capture threshold energy. $F(\pm Z,\Psi)$ are the Fermi functions and $D_\pm$ are the lepton distribution functions. For further details, we refer to Ref. [61].

III. RESULTS AND DISCUSSION

As discussed earlier, the current study investigates the effect of nuclear shape and pairing gaps on calculated γ-heating rates in astrophysical environment. Our ensemble consist of top 100 EC nuclei, covering the range $A = 48$ - 87 and $Z = 21$ - 36, and based on the recent rankings published by Nabi et al. [49]. We employed four distinct pairing gaps: $\Delta^{(4)}$, $\Delta^{(5)}$, $\Delta^{(LN)}$ and $\Delta^{(MN)}$ and three nuclear deformation parameter sets derived from the β_2 [FRLDM (1981)], β_2 [FRDM (1992)] and the β_2 [FRDM (2012)] in our investigation.

Fig. 1 presents the calculated ground-state Gamow–Teller (GT) strength functions for ^{51}Cr, ^{56}Ni, ^{57}Co and ^{64}Cu, examined using the pn-QRPA framework by employing the selected sets of nuclear deformation and pairing gap values. Our model calculated GT strength distributions are further compared with the available experimental data [62]. This comparison provides an opportunity to gauge the performance of our chosen nuclear model. Fig. 1 reflects the sensitivity of transition strengths to both pairing correlations and quadrupole deformations. The abscissa shows the daughter excitation energies up to the Q-values. The experimental data [62] were reported up to 0.75240 MeV, 2.13290 MeV, 0.83232 MeV and 1.67460 MeV for ^{51}Cr, ^{56}Ni, ^{57}Co and ^{64}Cu, respectively.

The measured data for ^{51}Cr exhibits two low-lying GT transitions at the ground state and at $E_x \approx 0.32$ MeV, indicating a simple single-particle configuration, consistent with the odd-proton character of ^{51}Cr in the lower-fp shell. The pn-QRPA calculations successfully reproduced the two GT transitions. The $\Delta^{(LN)}$ model provided the best agreement with experimental values, with $B(\mathrm{GT}) = 1.633\times10^{-2}$ MeV^{-1} and 5.52×10^{-3} MeV^{-1}, respectively. The improved correspondence results from the Lipkin–Nogami particle-number projection [50], which stabilizes pairing correlations and reduces artificial level fluctuations. The $\Delta^{(MN)}$ prescription enhanced the overall transition strength ($B(\mathrm{GT}) = 2.68\times10^{-2}$ MeV^{-1} and 7.27×10^{-3} MeV^{-1}), consistent with the stronger mass-scaled pairing field introduced by Madland and Nix [51]. The FRDM (1992) deformation resulted in higher magnitude of GT strengths. The FRDM (2012) deformation, incorporating updated microscopic corrections, produced the most balanced results. Experimentally, ^{56}Ni exhibits a

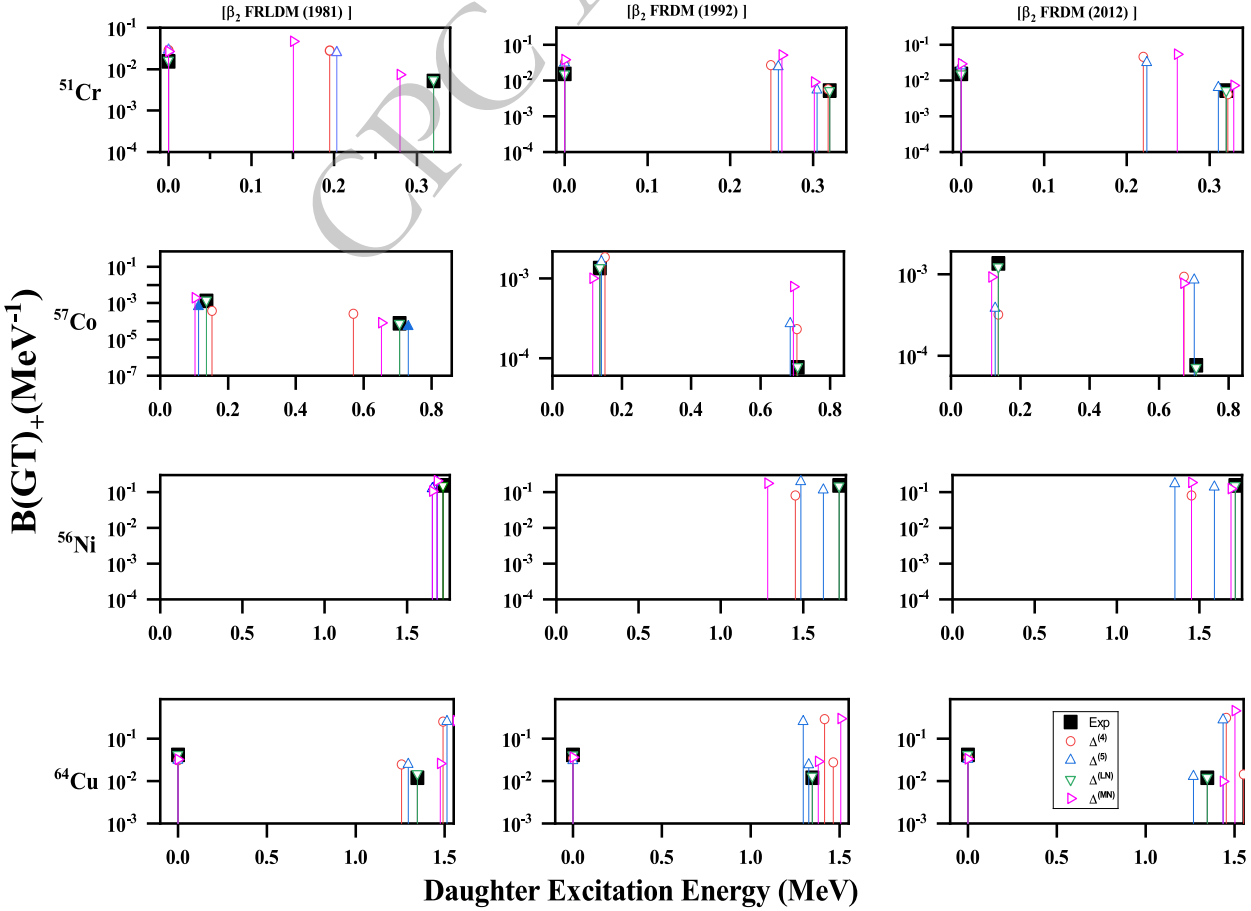

Fig. 1. (color online) Comparison of ground-state GT strength distributions for ^{51}Cr, ^{56}Ni, ^{57}Co and ^{64}Cu, using three distinct nuclear deformation values and four different pairing gap schemes, with experimental data [62].

prominent GT transition centered at $E_x \approx 1.72$ MeV with a strength of $B(\mathrm{GT}) = 1.5177 \times 10^{-1}$ MeV^{-1}. This strong, low-lying transition reflects the doubly magic, closed-shell configuration ($Z = N = 28$). The overall fragmentation pattern is minimal, consistent with the low collectivity expected for a near spherical nucleus. Our model reproduced the strong single GT transition reasonably well, though small quantitative differences appear due to the sensitivity of closed-shell nuclei to the choice of pairing and deformation parameters. ^{57}Co exhibits two low-lying GT transitions around $E_x \approx 0.14$ MeV and 0.71 MeV, with corresponding B(GT) strengths 1.35×10^{-3} MeV^{-1} and 7.606×10^{-5} MeV^{-1}, respectively. These weak transitions are consistent with the odd-proton configuration of ^{57}Co. The pn-QRPA results were in overall good comparison with the measured data. The odd-odd nucleus ^{64}Cu displays two dominant GT transitions: ground state and at $E_x \approx 1.35$ MeV. The significant ground-state component and the moderately strong excited transition indicate a mixture of single-particle and weakly collective GT configurations, consistent with the odd–odd nature of ^{64}Cu. The pn-QRPA results reproduce these two transitions fairly well for all input parameters. The combination of FRDM (2012) deformation values and $\Delta^{(\mathrm{LN})}$ pairing gaps provided the closest agreement with measured data for the four selected nuclei.

The main feature of the current study is a comprehensive analysis of γ-heating rates resulting from electron capture processes in astrophysical environments. Figs. 2 - 7 examine the sensitivity of these rates to nuclear pairing gaps and ground-state deformations. Our calculations span the temperature range (1–10) GK and density range (10^9–10^{11}) g/cm^3. We compare our calculated results with available shell model (SM) γ-ray heating rates [63], as presented in Figs. (2 - 7). The authors of Ref. [63] highlighted the critical issue of electron chemical potential and Q-values in electron-capture transitions of fp-shell nuclei. They incorporated electron screening effects in their calculations of electron-capture rates. Screening increases the electron fraction while simultaneously lowering the capture rates. In Ref. [63], the authors adopted the electron-capture rates for fp-shell nuclei from Honma et al. [64], whereas for other nuclei they employed the rates reported in Refs. [41, 65, 66].

The empirical pairing gaps, $\Delta^{(4)}$ and $\Delta^{(5)}$, generally predict comparable γ-heating rates (within a factor of 2–3), with $\Delta^{(5)}$ resulting in slightly enhanced rates at higher temperatures ($T \geq 10$ GK). This similarity reflects their common theoretical foundation in finite-difference approximations of the pairing gap, with the $\Delta^{(5)}$ method

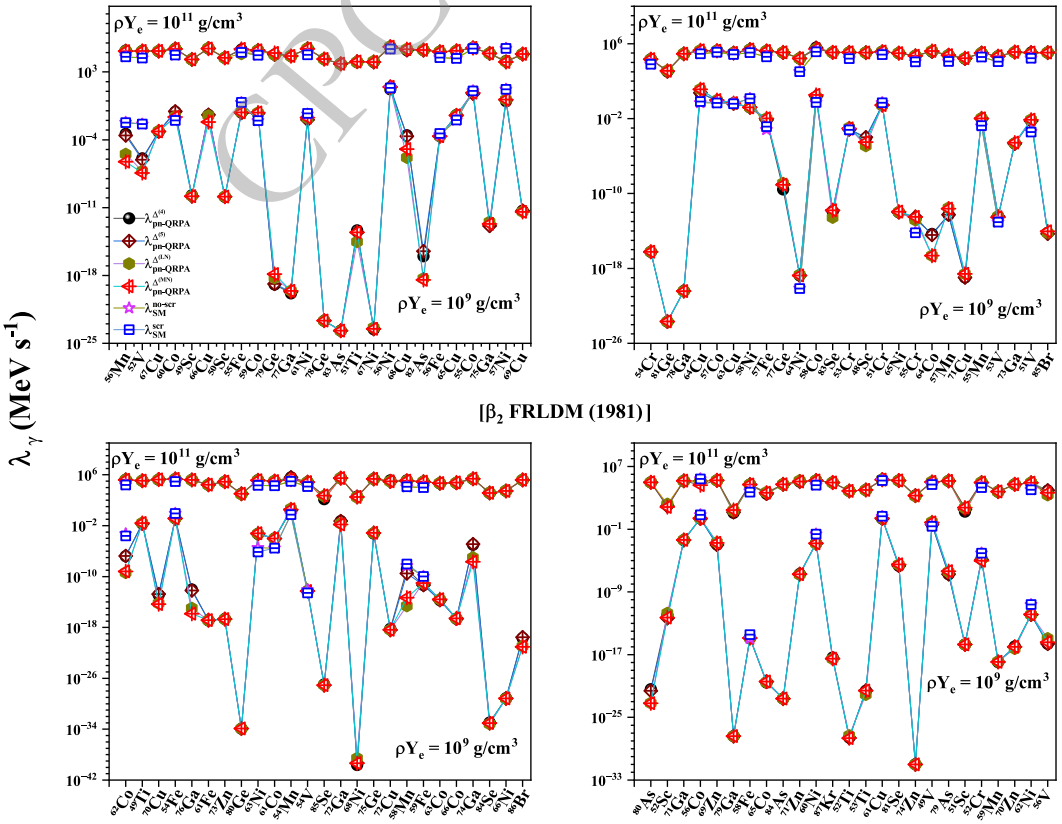

Fig. 2. (color online) The pn-QRPA calculated γ -heating rates ({MeV.s $^{-1}$ }) for the top 100 EC nuclei at $T = 1$ GK calculated using four different pairing gaps and β_2 [FRLDM (1981)] as input parameters. Shown also are the shell model rates with and without screening effects [63].

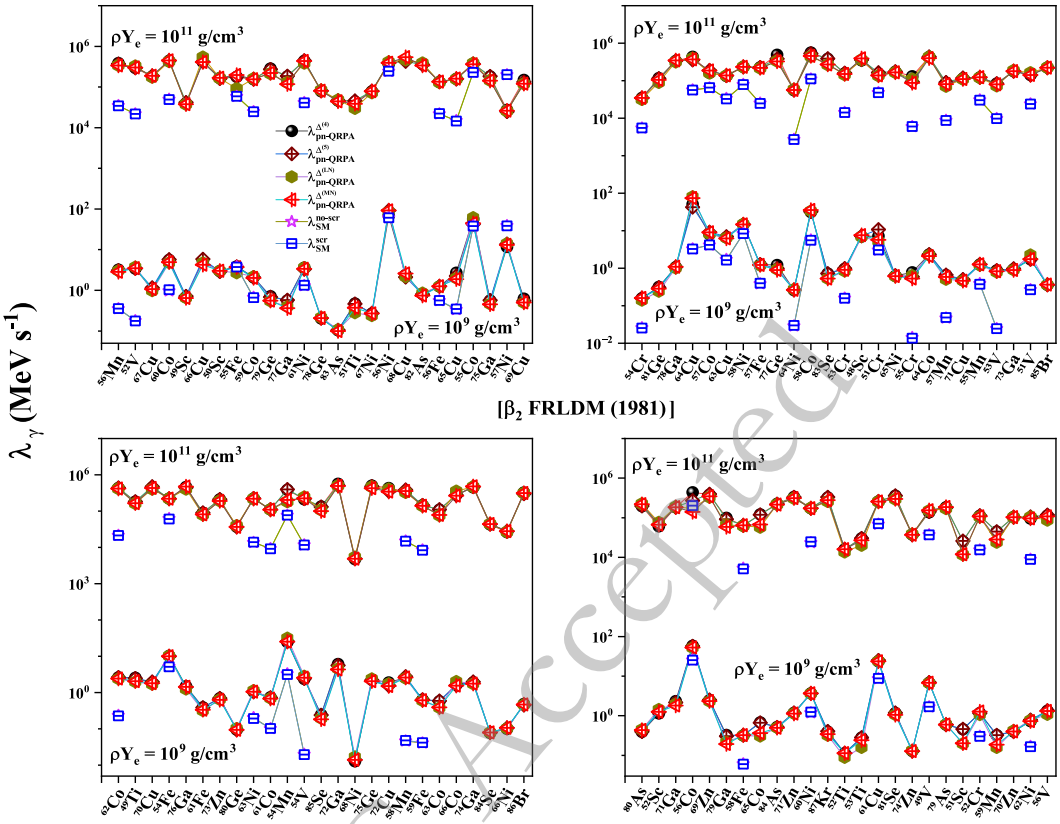

Fig. 3. (color online) Same as Fig. 2 but at $T = 10$ GK.

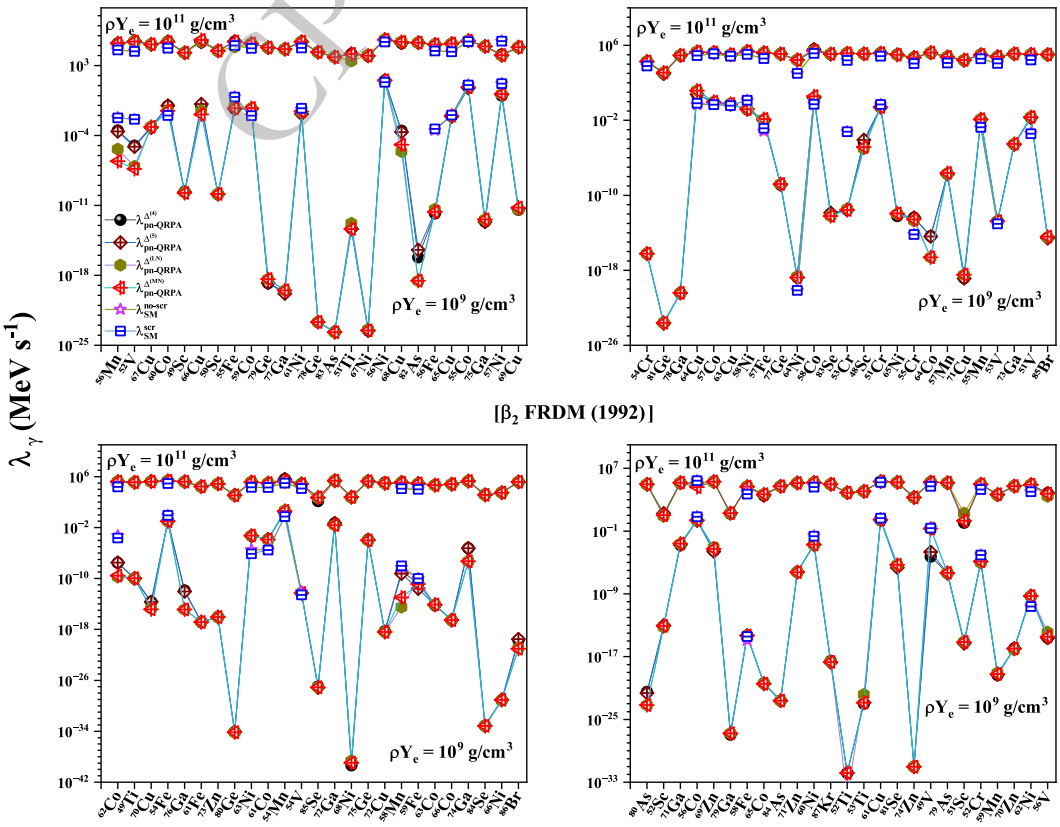

Fig. 4. (color online) Same as Fig. 2 ($T = 1$ GK) but using β_2 [FRDM (1992)] as input parameter in the pn-QRPA rates.

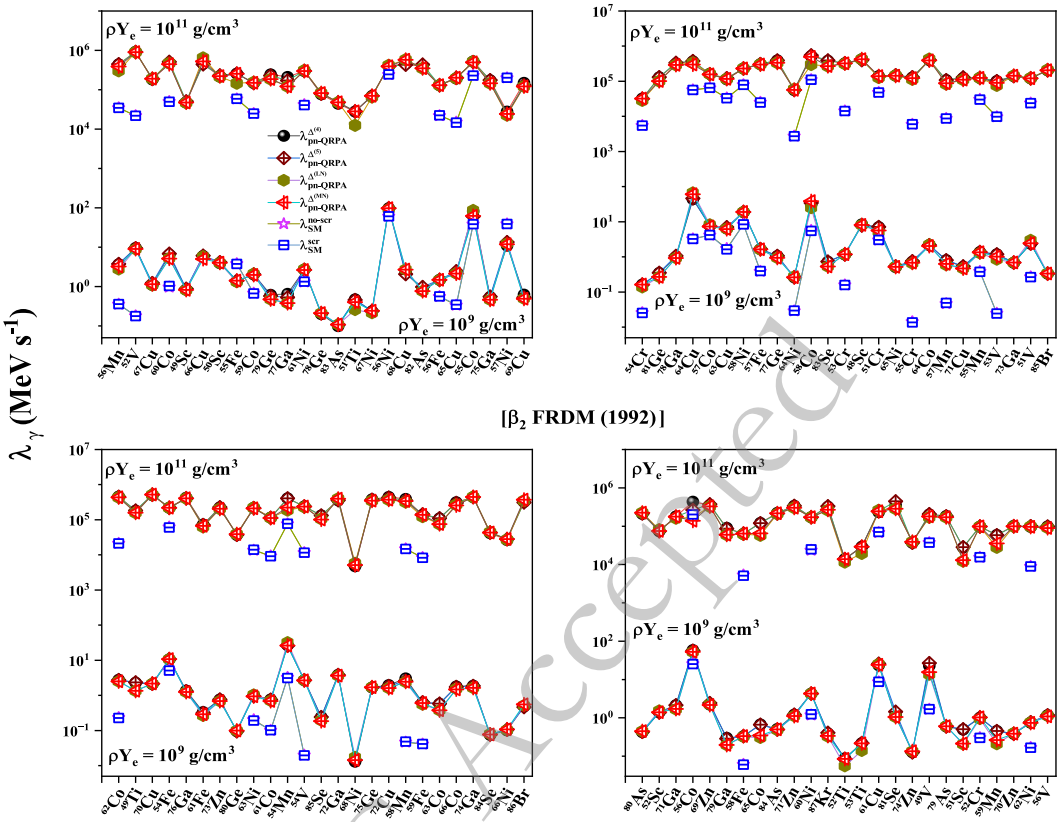

Fig. 5. (color online) Same as Fig. 4 but at $T = 10$ GK.

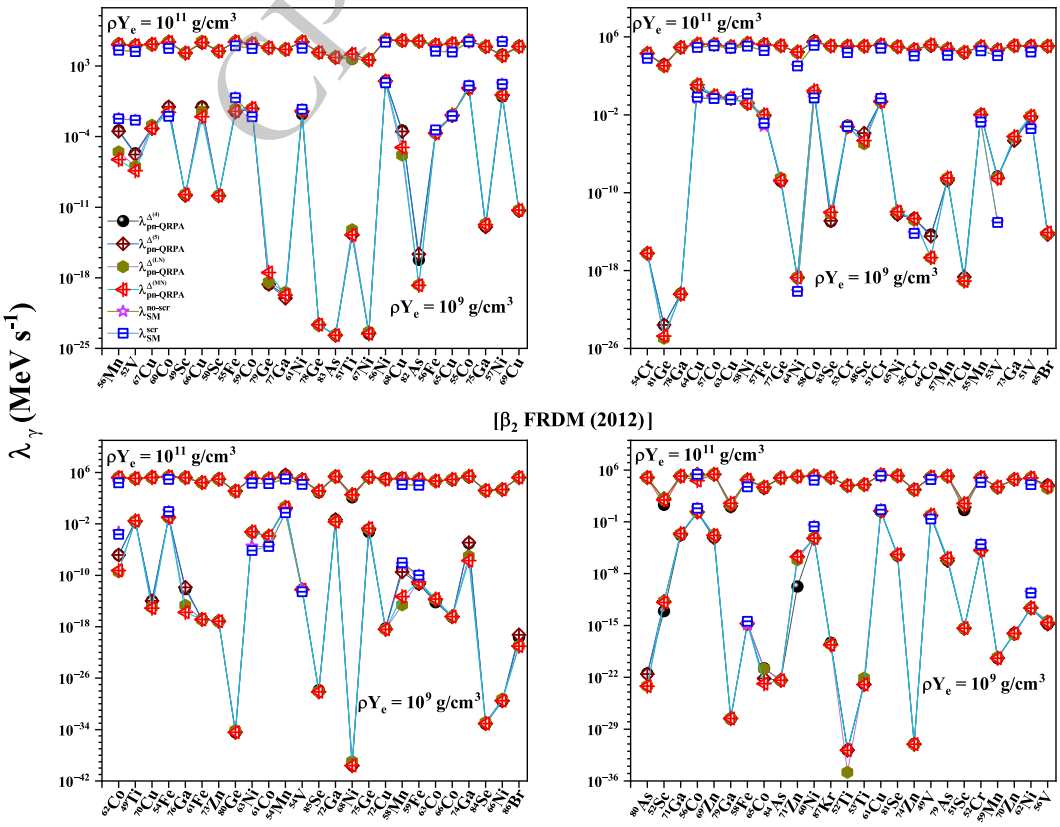

Fig. 6. (color online) Same as Fig. 2 ($T = 1$ GK) but using β_2 [FRDM (2012)] as input parameter in the pn-QRPA rates.

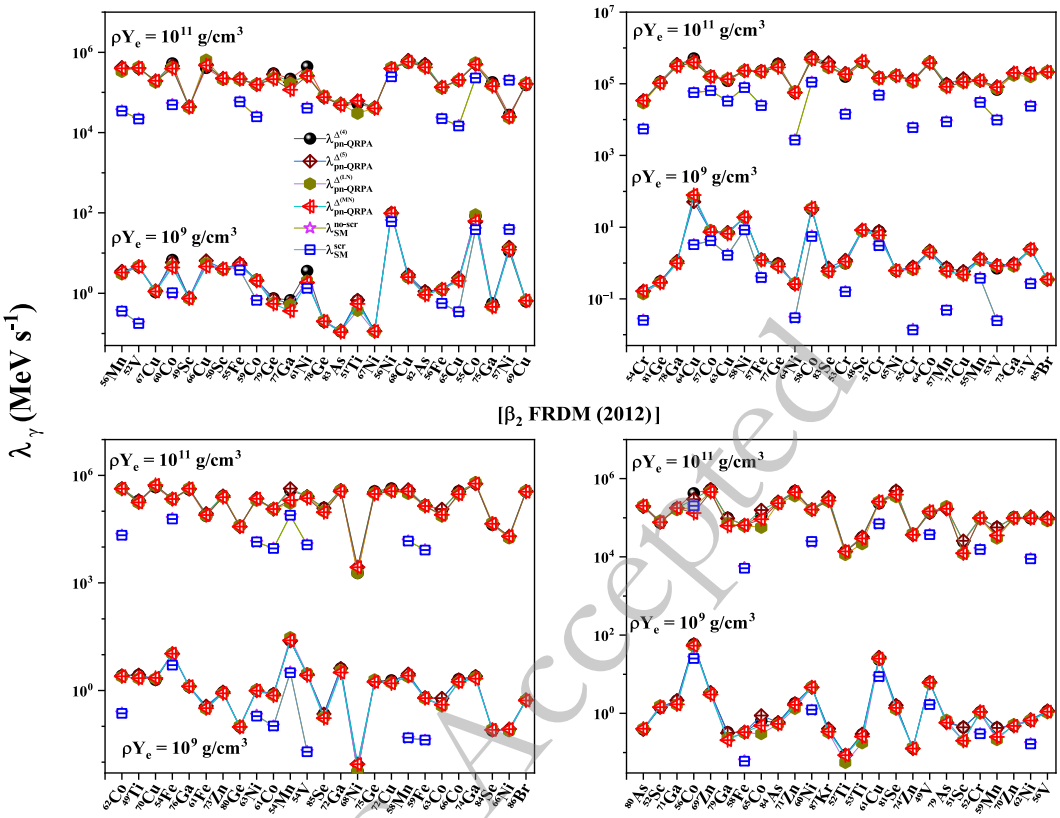

Fig. 7. (color online) Same as Fig. 6 but at $T = 10\ GK$.

providing modest improvement through reduced sensitivity to single-level fluctuations. In contrast, the $\Delta^{(LN)}$ approach demonstrates markedly different behavior. The $\Delta^{(LN)}$ predicted γ-heating rates are around an order of magnitude smaller than those predicted by the empirical pairing gaps. This suppression stems from the method's treatment of particle-number conservation and inclusion of higher-order correlations, which significantly alter the predicted phase space for electron capture transitions. The $\Delta^{(MN)}$ model frequently resulted in intermediate values of γ-heating rates, between the finite-difference methods and the Lipkin–Nogami approach.

For the majority of nuclei, under low-temperature and low-density conditions ($T = 1$ GK, $\rho = 10^7$ g/cm^3), the γ-heating rates are negligibly small [$\sim (10^{-40}$ - $10^{-10})$ MeV s^{-1}]. Under these physical conditions, excited states are not appreciably populated, and electron capture proceeds primarily from the parent ground state, often resulting in low-energy transitions or stable daughter nuclei, yielding little γ-ray heating.

On the other extreme, for selected high-temperature and high-density regions ($T = 10$ GK, $\rho = 10^{11}$ g/cm^3), the electron chemical potentials exceed typical nuclear Q-values. Under such extreme conditions, the sensitivity of γ-heating rates to pairing gaps diminishes considerably. The increased phase space for electron capture overwhelms subtle differences in nuclear structure, leading to convergence of predictions across varying pairing gaps. All models converge to similar magnitudes $\sim (10^4$–$10^5)$ MeV s^{-1}], suggesting reduced sensitivity to pairing treatment under extreme conditions where thermal effects dominate.

The progression from β_2 [FRLDM (1981)] to β_2 [FRDM (1992)] and finally to β_2 [FRDM (2012)] bears consequences for γ-ray heating rate predictions due to substantial theoretical improvements in the treatment of nuclear deformations, particularly for neutron-rich nuclei and those with soft potential energy surfaces. The FRDM (2012) model incorporates a more sophisticated description of deformation energy surfaces and includes a density-symmetry coefficient L that was previously set to zero. These improvements particularly affect nuclei with soft potential energy surfaces, where small changes in the deformation energy landscape may alter the predicted ground-state deformations. For a realistic simulation of superbursts and post-silicon burning phases of stars, it is recommended to employ the FRDM (2012) deformation parameters together with $\Delta^{(LN)}$ pairing gaps because they provide the best prediction power to our nuclear model.

Tables 1-2 present the ratio of pn-QRPA calculated mean γ-heating rates to those obtained from SM calculations [63]. The ratios are shown for the pn-QRPA rates using different choices of pairing gaps and nuclear deformations. Table (1) shows the computed ratio with the

Table 1. Comparison of the reported pn-QRPA calculated mean γ -heating rates with shell model rates excluding screening effects [63].

$T(GK)$	β_2 [FRLDM (1981)]							
	$\rho Y_e = 10^9\ g/cm^3$				$\rho Y_e = 10^{11}\ g/cm^3$			
	$\frac{\bar{\lambda}^{\Delta^{(4)}}_{pnQRPA}}{\bar{\lambda}^{no-scr}_{SM}}$	$\frac{\bar{\lambda}^{\Delta^{(5)}}_{pnQRPA}}{\bar{\lambda}^{no-scr}_{SM}}$	$\frac{\bar{\lambda}^{\Delta^{(LN)}}_{pnQRPA}}{\bar{\lambda}^{no-scr}_{SM}}$	$\frac{\bar{\lambda}^{\Delta^{(MN)}}_{pnQRPA}}{\bar{\lambda}^{no-scr}_{SM}}$	$\frac{\bar{\lambda}^{\Delta^{(4)}}_{pnQRPA}}{\bar{\lambda}^{no-scr}_{SM}}$	$\frac{\bar{\lambda}^{\Delta^{(5)}}_{pnQRPA}}{\bar{\lambda}^{no-scr}_{SM}}$	$\frac{\bar{\lambda}^{\Delta^{(LN)}}_{pnQRPA}}{\bar{\lambda}^{no-scr}_{SM}}$	$\frac{\bar{\lambda}^{\Delta^{(MN)}}_{pnQRPA}}{\bar{\lambda}^{no-scr}_{SM}}$
1	7.86	8.16	8.75	9.76	4.44	4.38	4.20	4.31
3	6.39	6.57	7.37	7.22	4.63	4.61	4.46	4.59
10	11.56	11.38	11.87	11.33	8.76	8.71	8.41	8.42
	β_2 [FRDM (1992)]							
1	10.41	10.23	10.73	10.94	4.61	4.63	4.39	4.49
3	6.30	6.33	6.97	6.83	5.31	5.31	5.05	5.18
10	13.74	13.65	12.65	12.87	10.07	10.08	9.33	9.62
	β_2 [FRDM (2012)]							
1	8.29	8.08	9.00	9.40	4.45	4.41	4.24	4.30
3	6.99	7.00	7.73	7.39	4.82	4.80	4.64	4.72
10	12.42	12.67	12.23	12.05	9.14	9.28	8.64	8.83

Table 2. Comparison of the reported pn-QRPA calculated mean γ -heating rates with shell model rates including screening effects [63].

$T(GK)$	β_2 [FRLDM (1981)]							
	$\rho Y_e = 10^9\ g/cm^3$				$\rho Y_e = 10^{11}\ g/cm^3$			
	$\frac{\bar{\lambda}^{\Delta^{(4)}}_{pnQRPA}}{\bar{\lambda}^{scr}_{SM}}$	$\frac{\bar{\lambda}^{\Delta^{(5)}}_{pnQRPA}}{\bar{\lambda}^{scr}_{SM}}$	$\frac{\bar{\lambda}^{\Delta^{(LN)}}_{pnQRPA}}{\bar{\lambda}^{scr}_{SM}}$	$\frac{\bar{\lambda}^{\Delta^{(MN)}}_{pnQRPA}}{\bar{\lambda}^{scr}_{SM}}$	$\frac{\bar{\lambda}^{\Delta^{(4)}}_{pnQRPA}}{\bar{\lambda}^{scr}_{SM}}$	$\frac{\bar{\lambda}^{\Delta^{(5)}}_{pnQRPA}}{\bar{\lambda}^{scr}_{SM}}$	$\frac{\bar{\lambda}^{\Delta^{(LN)}}_{pnQRPA}}{\bar{\lambda}^{scr}_{SM}}$	$\frac{\bar{\lambda}^{\Delta^{(MN)}}_{pnQRPA}}{\bar{\lambda}^{scr}_{SM}}$
1	20.8	20.2	22.1	25.1	4.51	4.44	4.27	4.37
3	6.94	7.17	7.90	7.83	4.69	4.67	4.52	4.65
10	11.6	11.4	11.9	11.3	8.76	8.71	8.41	8.42
	β_2 [FRDM (1992)]							
1	23.2	22.4	24.1	25.0	4.68	4.69	4.45	4.56
3	6.88	6.92	7.53	7.39	5.37	5.36	5.11	5.24
10	13.8	13.7	12.7	12.9	10.1	10.1	9.33	9.61
	β_2 [FRDM (2012)]							
1	21.1	20.6	22.5	24.0	4.52	4.47	4.30	4.36
3	7.69	7.73	8.41	8.07	4.88	4.86	4.70	4.78
10	12.4	12.7	12.3	12.1	9.13	9.27	8.64	8.83

SM calculations excluding screening effects. The pn-QRPA rates are bigger than the SM rates roughly by an order of magnitude at high temperatures. At $T = (1–3)$ GK and $\rho Y_e = 10^{11}\ g/cm^3$, the pn-QRPA rates are around factor (4–5) bigger than the SM rates. Table (2) shows that the screening effects in the SM calculation are highest at low temperature ($T = 1\ GK$) and low density ($\rho Y_e = 10^9\ g/cm^3$) where the SM rates reduces up to a factor of 2.6. Under such physical conditions, the pn-QRPA rates are up to factor 25 bigger than the corresponding SM rates. The comparison at higher density ($\rho Y_e = 10^{11}\ g/cm^3$) is akin to that exhibited in Table 1.

We wanted to find out the maximum change in the calculated γ-heating rates as a result of changing pairing gaps and nuclear deformation values. It is noted that for computed γ-heating rates bearing negative exponents, orders of magnitude changes may arise due to a small variation in model input parameters but they are hardly of any significance in simulation studies due to their almost zero impact. Fig. 8 shows computed γ-heating rates at a

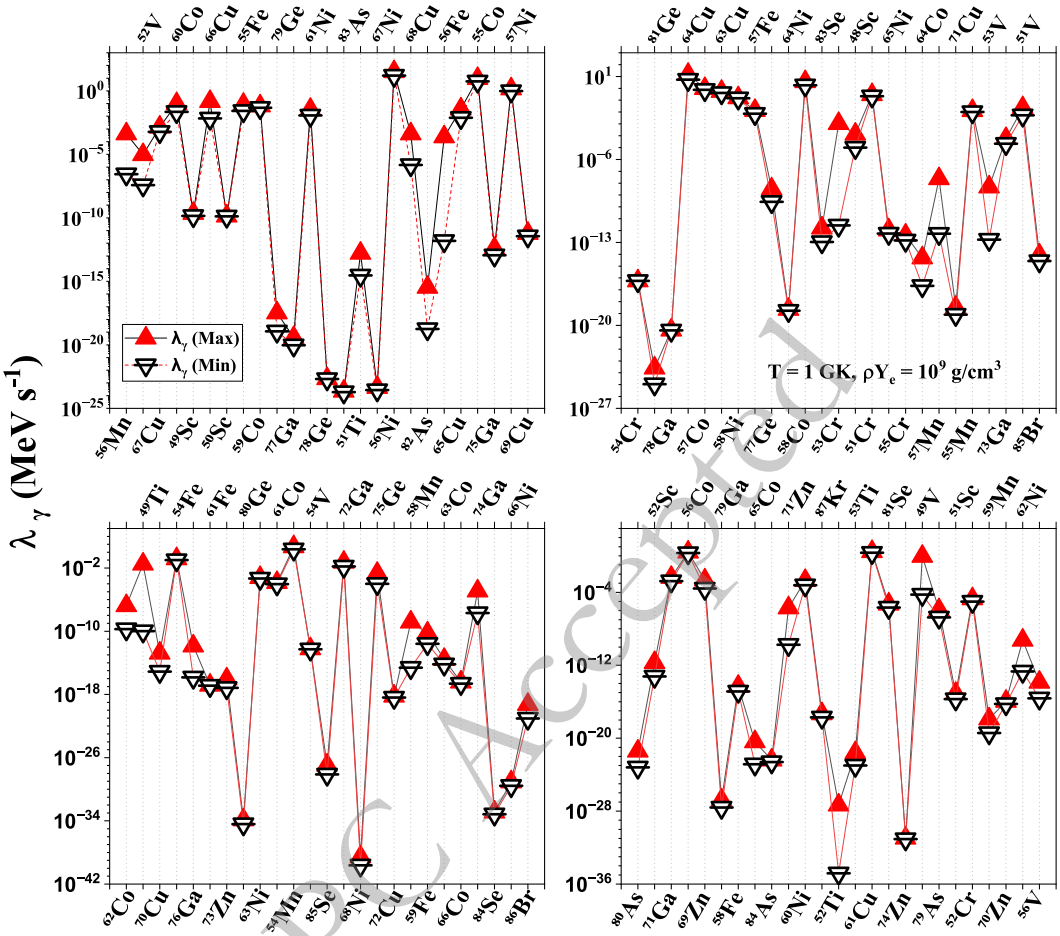

Fig. 8. (color online) Maximum and minimum calculated γ -ray heating rates (MeV s^{-1}) by changing pairing gaps and deformations for the top 100 EC nuclei under superburst conditions.

density of 10^9 g/cm^3 and temperature of $T = 1$ GK. These conditions correspond to the physical environment of superbursts in accreting neutron stars [4]. The spread in γ-heating rates is obtained by varying the nuclear deformation parameter β_2 and different prescriptions for the pairing gaps, highlighting the sensitivity of weak-interaction rates to nuclear structure inputs. From a physical perspective, nuclear deformation modifies single-particle level densities and transition strengths, while pairing correlations alter the availability of quasiparticle states. These effects directly influence electron-capture chains and associated γ-emission, which are key contributors to crustal heating.

In order to make the analysis more meaningful, Fig. 9 displays top three cases where maximum change of heating rate occurs for nuclei possessing γ-heating rates of magnitude bigger than 1 MeV s^{-1}. Fig. 9 illustrates the maximum change in the calculated γ-heating rates as a result of changing either the pairing gaps or deformation values. It is noted from Fig. 9 that changing β_2 values have a bigger effect on computed heating rates when compared with changing pairing gaps. The γ-heating rates change up to a factor of 26 and 16 by changing the deformation and pairing gap values, respectively. The left panel of Fig. 9 shows maximum variation in computed heating rates when we altered the pairing gaps in our nuclear model. For ^{51}Sc, a factor 16 change in γ-heating rates was noted at $T = 1$ GK, $\rho = 10^{11}$ g/cm^3. For the remaining two nuclei, ^{51}Ti ($T = 1$ GK, $\rho = 10^{11}$ g/cm^3) and ^{56}Co ($T = 3$ GK, $\rho = 10^{11}$ g/cm^3) the heating rate changed by a factor of (4 - 5). The right panel, on the other hand, displays the maximum change in computed γ-heating rates when we varied the β_2 values. A maximum change of factor 26 was noted for the case of ^{51}Sc ($T = 1$ GK, $\rho = 10^{11}$ g/cm^3). More than an order of magnitude change in heating rates was also computed for ^{49}V ($T = 10$ GK, $\rho = 10^9$ g/cm^3) and ^{52}Sc ($T = 1$ GK, $\rho = 10^{11}$ g/cm^3) as a result of changing β_2 values. A more refined inspection reveals that the calculated γ-heating rates are a sensitive function of both the pairing gaps and deformations when a nucleus approaches a magic proton, magic neutron, or a magic mass number. Near these shell closures, nuclei tend to favor spherical configurations, and even a minute departure of β_2 from zero can induce substantial modific-

ations in the predicted heating rates. The intensity of the pairing interaction within a nucleus is primarily governed by the residual pairing correlations and the density of single-particle levels in the vicinity of the Fermi surface. As nuclei near magic numbers undergo structural rearrangements in their Fermi surfaces, alterations in the pairing gaps can exert a pronounced influence on the resulting γ-heating rates.

Fig. 10 presents the calculated γ-heating rates averaged over the selected 100 nuclei and presented as snapshots of predetermined temperature and density values. For stellar temperatures [$T = (1–3)$ GK], the heating rates remain minimal, typically in the range of $(10^{-5}–10^{-4})$ MeV s^{-1} at low density of 10^7 g cm^{-3}. At high temperature ($T = 10$ GK) and density ($\rho Y_e = 10^{11}$ g cm^{-3}), the rates increase by several orders of magnitude, reaching

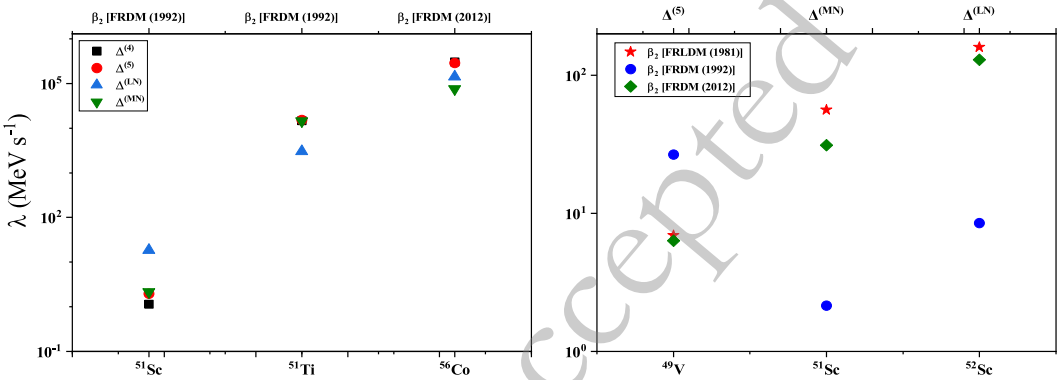

Fig. 9. (color online) Top three variations in the calculated γ-heating rates of magnitude bigger than 1 MeV s^{-1} with changing input parameters. For physical conditions see text.

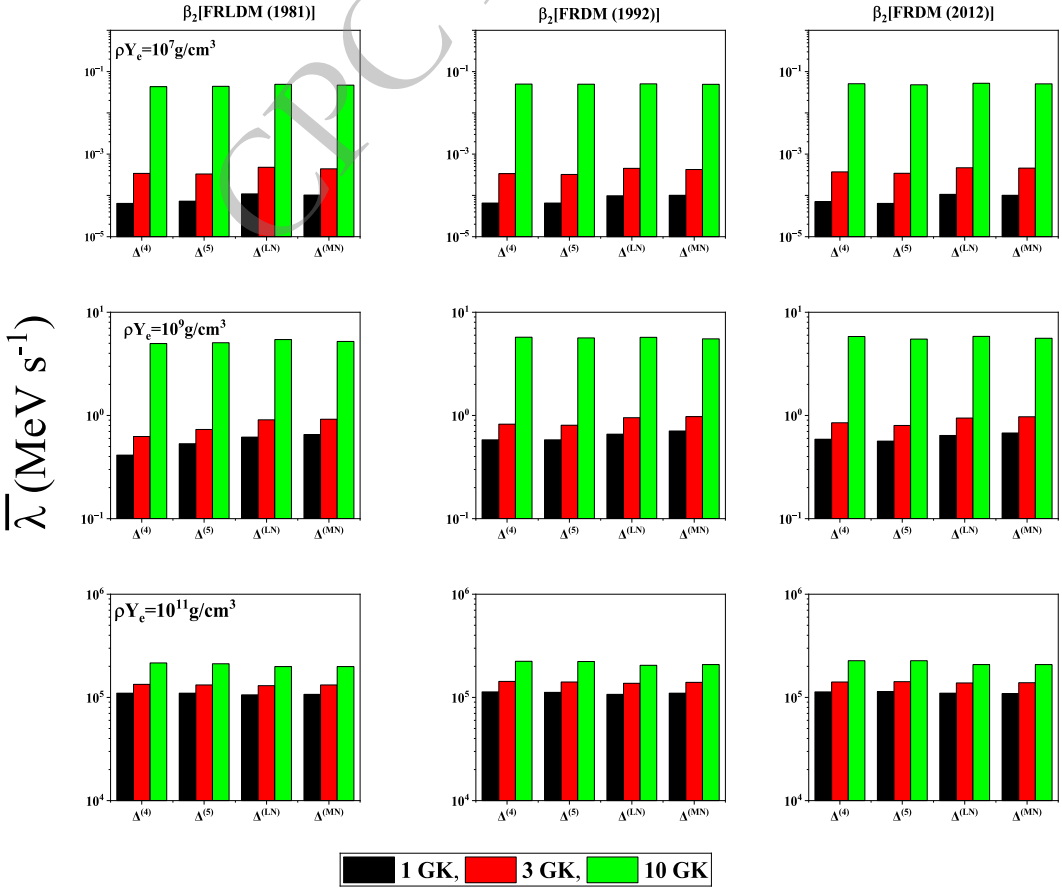

Fig. 10. (color online) Comparison of calculated γ-ray heating rates (MeV s^{-1}) averaged over the selected top 100 EC nuclei, as a function of pairing gaps and deformations.

values in the range (10^4-10^5) MeV s^{-1}. This enhancement is attributed to the growing contribution of thermally populated excited states. At a given temperature, γ-ray heating rates increase monotonically with density. High-density environments increase the Fermi energy values (up to 24 MeV) thereby enhancing electron captures to excited states by orders of magnitude and subsequent γ-emissions. The β_2 [FRLDM (1981)] resulted in comparatively lower heating rates at temperatures [$T = (1-3)$ GK] followed by the β_2 [FRDM (1992)] rates. The β_2 [FRDM (2012)] provided the highest γ-heating rates, highlighting the revised microscopic corrections which resulted in enhanced transition rates. Pairing gap variations influence the predicted heating rates to a lesser extent. For temperatures around 10 GK, and for all density regions covered in the current investigation, the highest average heating rate of $\bar{\lambda}_\gamma = 2.27\times10^5$ MeV s^{-1} resulted from the $\Delta^{(4)}/\Delta^{(5)}$ pairing gap formula and FRDM (2012) nuclear deformation parameters. Under superburst ignition conditions, our nuclear model predicted a maximum and minimum mean γ-heating rates of $\bar{\lambda}_\gamma = 7.08\times10^{-1}$ MeV s^{-1} and $\bar{\lambda}_\gamma = 4.13\times10^{-1}$ MeV s^{-1}, respectively, for the top 100 EC nuclei selected in our investigation. The maximum mean heating rates were predicted using the $\Delta^{(MN)}$ pairing gap and nuclear deformation parameters from the FRDM (1992) model. The minimum γ-heating rates resulted by employing the $\Delta^{(4)}$ pairing gap and β_2 values from the FRLDM (1981) model.

IV. CONCLUSIONS

In this study, we presented calculations of the γ-heating rates due to weak interaction decays in stellar matter. Our pool of nuclei consisted of top 100 EC nuclei possessing astrophysical importance. These nuclei were selected based on their respective contribution to the time rate of change of the lepton fraction ($\dot{Y}_e$) during presupernova evolution, as identified in a recent simulation study [49]. A key feature of our computation was the microscopic calculation of GT strength distributions for both ground and excited states. Pairing gaps and nuclear deformations serve as essential model parameters for calculation of nuclear structure properties. The current investigation highlighted that changing pairing gaps and nuclear deformation values influenced the GT strength distributions and associated γ-heating energy rates. For low-density and low-temperature regions, the lowest mean heating rate of $\bar{\lambda}_\gamma = 6.39\times10^{-5}$ MeV s^{-1} was recorded for $\Delta^{(4)}$ pairing gaps and FRLDM (1981) nuclear deformations. For high-density and high-temperature zones, the highest mean heating rate of $\bar{\lambda}_\gamma = 2.27\times10^5$ MeV s^{-1} was computed for $\Delta^{(4)}/\Delta^{(5)}$ pairing gaps and FRDM (2012) nuclear deformations. The calculated γ-heating rates changed by up to a factor 26 by a change in deformation values. Altering pairing gaps changed the heating rates up to a factor of 16. These changes bear significance in reducing the ignition depths of superbursts and counteracting the reduction in crust temperature resulting from Cooper pair neutrino emissions. Our results suggest that nuclear structure properties can significantly alter the intensity of crustal heating. In particular, the interplay between pairing gap prescriptions and deformation parameters may shape the microscopic heating profiles and thermal evolution of accreting neutron star crusts.

References

[1] H. A. Bethe, Phys. Rev. **55**, 434 (1939)
[2] E. M. Burbidge, G. R. Burbidge, W. A. Fowler, *et al.*, Rev. Mod. Phys. **29**, 547 (1957)
[3] W. Baade and F. Zwicky, Proc. Natl. Acad. Sci. USA **20**, 259 (1934)
[4] A. Cumming, J. Macbeth, and D. Page, Astrophys. J. **646**, 429 (2006)
[5] E. Flowers, M. Ruderman, and P. Sutherland, Astrophys. J. **205**, 541 (1976)
[6] S. Gupta, E. F. Brown, H. Schatz, *et al.*, Astrophys. J. **662**, 1188 (2007)
[7] H. A. Bethe, G. E. Brown, J. Applegate, *et al.*, Nucl. Phys. A **324**, 487 (1979)
[8] S. Usman and A. Mushtaq, Sci. Rep. **13**, 15315 (2023)
[9] H.T. Janka, K. Langanke, A. Marek, *et al.*, Phys. Rep. **442**, 38 (2007)
[10] B. Pritychenko, M. Birch, B. Singh, *et al.*, At. Data Nucl. Data Tables **107**, 1 (2016)
[11] N. J. Stone, At. Data Nucl. Data Tables **111**, 1 (2016)
[12] K. Zhang, M. K. Cheoun, Y. B. Choi, *et al.*, At. Data Nucl. Data Tables **144**, 101488 (2022)
[13] P. Guo, X. Cao, K. Chen, *et al.*, At. Data Nucl. Data Tables **158**, 101661 (2024)
[14] M. Bender, P.-H. Heenen, and P.-G. Reinhard, Rev. Mod. Phys. **75**, 121 (2003)
[15] J. M. Lattimer, K. A. van Riper, M. Prakash, *et al.*, Astrophys. J. **425**, 802 (1994)
[16] D. Page and S. Reddy, in Neutron Star Crust, edited by C. A. Bertulani and J. Piekarewicz (Nova Publishers, 2012), p. 281
[17] J. Piekarewicz, F. J. Fattoyev, and C. J. Horowitz, Phys. Rev. C **90**, 015803 (2014)
[18] X. Shang and A. Li, Astrophys. J. **923**, 108 (2021)
[19] U. Lombardo, H. Schulze, C. W. Shen, *et al.*, Int. J. Mod. Phys. E **14**, 513 (2005)
[20] H. Wibowo, E. Litvinova, Y. Zhang, *et al.*, Phys. Rev. C **102**, 054321 (2020)
[21] E. Yüksel, Nucl. Phys. A **1014**, 122238 (2021)
[22] R. Lisboa, M. Malheiro, and B. V. Carlson, Phys. Rev. C **93**, 024321 (2016)
[23] Y. F. Niu, Z. M. Niu, N. Paar, *et al.*, Phys. Rev. C **88**, 034308 (2013)
[24] N. D. Dang and A. Arima, Phys. Rev. C **68**, 044303 (2003)
[25] Y. F. Niu, N. Paar, D. Vretenar, *et al.*, Phys. Lett. B **681**,

315 (2009)
[26] E. Litvinova and P. Schuck, Phys. Rev. C **104**, 044330 (2021)
[27] H. Wibowo and E. Litvinova, Phys. Rev. C **106**, 044304 (2022)
[28] L. G. Moretto, Phys. Lett. B **40**, 1 (1972)
[29] N. D. Dang, P. Ring, and R. Rossignoli, Phys. Rev. C **47**, 606 (1993)
[30] V. Zelevinsky, B. A. Brown, N. Frazier, *et al*., Phys. Rep. **276**, 85 (1996)
[31] A. Volya, B. A. Brown, and V. Zelevinsky, Phys. Lett. B **509**, 37 (2001)
[32] A. Ravlić, E. Yüksel, T. Nikšić, *et al*., Nat. Commun. **14**, 4834 (2023)
[33] N. D. Dang, K. Tanabe, and A. Arima, Nucl. Phys. A **675**, 531 (2000)
[34] J.-U. Nabi and H. V. Klapdor-Kleingrothaus, Eur. Phys. J. A **5**, 337 (1999)
[35] A. A. Dzhioev, K. Langanke, G. Martínez-Pinedo, *et al*., Phys. Rev. C **101**, 025805 (2020)
[36] E. Yüksel, N. Paar, G. Colò, *et al*., Phys. Rev. C **101**, 044305 (2020)
[37] A. F. Fantina, E. Khan, G. Colò, *et al*., Phys. Rev. C **86**, 035805 (2012)
[38] E. Litvinova and C. Robin, Phys. Rev. C **103**, 024326 (2021)
[39] E. Yüksel, N. Paar, G. Colò, *et al*., Phys. Rev. C **101**, 044305 (2020)
[40] G. M. Fuller, W. A. Fowler, and M. J. Newman, Astrophys. J. Suppl. Ser. **42**, 447 (1980)
[41] G. M. Fuller, W. A. Fowler, and M. J. Newman, Astrophys. J. Suppl. Ser. **48**, 279 (1982b)
[42] G. M. Fuller, W. A. Fowler, and M. J. Newman, Astrophys. J. **293**, 1 (1985)
[43] M. B. Aufderheide, I. Fushiki, S. E. Woosley, *et al*., Astrophys. J. Suppl. Ser. **91**, 389 (1994)
[44] K. Langanke and G. Martínez-Pinedo, Nucl. Phys. A **673**, 48 (2000)
[45] J. Pruet and G. M. Fuller, Astrophys. J. Suppl. Ser. **149**, 189 (2003)
[46] D. M. Brink, *The Influence of the Individual Nuclear Levels on the Widths of Nuclear Resonances*, D.Phil. thesis, University of Oxford (1955)
[47] P. Axel, Phys. Rev. **126**, 671 (1962)
[48] J.-U. Nabi, M. Nayab, and C. W. Johnson, J. Phys. G: Nucl. Part. Phys. **49**, 065201 (2022)
[49] J.-U. Nabi, A. Ullah, and A. A. Khan, Astrophys. J. **911**, 93 (2021)
[50] P. Möller, M. Mumpower, T. Kawano, *et al*., At. Data Nucl. Data Tables **125**, 1 (2019)
[51] D. G. Madland and J. R. Nix, Nucl. Phys. A **476**, 1 (1988)
[52] S. A. Changizi, C. Qi, and R. Wyss, Nucl. Phys. A **940**, 210 (2015)
[53] P. Möller and J. R. Nix, At. Data Nucl. Data Tables **26**, 165 (1981)
[54] P. Möller, J. R. Nix, W. D. Myers, *et al*., At. Data Nucl. Data Tables **59**, 185 (1995)
[55] P. Möller, A. J. Sierk, T. Ichikawa, *et al*., At. Data Nucl. Data Tables **109**, 1 (2016)
[56] K. Muto, E. Bender and H. V. Klapdor, Z. Phys. A **333**, 125 (1989)
[57] K. Nakamura, *et al*, J. Phys. G **37**, 075021 (2010)
[58] J. C. Hardy and I. S. Towner, Phys. Rev. C **79**, 055502 (2009)
[59] N. B. Gove and M. J. Martin, At. Data Nucl. Data Tables **10**, 205 (1971)
[60] J.-U. Nabi, A. Ullah, and M. A. Qammar, Nucl. Phys. A **2025**, 123237 (2025)
[61] J.-U. Nabi and H. V. Klapdor-Kleingrothaus, At. Data Nucl. Data Tables **88**, 237 (2004)
[62] National Nuclear Data Center (NNDC), Brookhaven National Laboratory, https://www.nndc.bnl.gov/, retrieved 26th September 2025
[63] K. Mori, T. Suzuki, M. Honma, *et al*., Astrophys. J. **904**, 29 (2020)
[64] M. Honma, T. Otsuka, T. Mizusaki, *et al*., J. Phys.: Conf. Ser. **20**, 7 (2005)
[65] G. M. Fuller, W. A. Fowler, and M. J. Newman, Astrophys. J. **252**, 715 (1982)
[66] T. Oda, M. Hino, K. Muto, *et al*., At. Data Nucl. Data Tables **56**, 231 (1994)